

## SOME PROBLEMS IN THE STUDY OF TRANSLUCENT CLOUDS USING SUN AUREOLE

A.A. Isakov

*Institute for Atmospheric Physics,  
Russian Academy of Sciences, Moscow  
Received December 11, 1996*

*The angular instrumental function of the sun aureole photometer is calculated for a set of scattering angles  $\varphi$ , and several kinds of the photometer geometry. The function takes into account the finiteness of angular dimensions of the sun and the device field of view. The equality of angular dimensions of the sun and the field of view is the condition of the optimum geometry. In this case, the instrumental function does not depend on the scattering angle  $\varphi$  in the range  $\varphi = 1-10^\circ$ , and the distortions of the aureole scattering phase functions detected  $\mu(\varphi, \lambda)$  are small. Numerical analysis of the sun spectrophotometer designed at the Institute for Atmospheric Physics demonstrates that the recorded  $\mu(\varphi, \lambda)$  contain information about particles of the size up to  $r \simeq 50-60 \mu\text{m}$  with moderate errors ( $\sim 10-15\%$ ). The data of two complex experiments in 1992 and 1994 have been inverted based on the analysis performed. It is established that relatively narrow single-mode particle size distributions prevail in the translucent clouds. The characteristic dimensions are  $r \simeq 15-50 \mu\text{m}$  in Ci clouds;  $r \simeq 20 \mu\text{m}$  for As clouds;  $r \simeq 2-3 \mu\text{m}$  for Ac clouds. The ice content was within the range  $1-30 \text{ g/m}^2$ . The distributions are multimode for the cases of multilayer cloudiness.*

### INTRODUCTION

It is well-known that particles with the characteristic size of a few tens of microns are present in cirrus clouds. Their relative content is sufficient to influence the clouds' optics significantly. This influence can be easily estimated by a narrow aureole created by a cirrus cloud around the moon. The angular size of the moon gives a frame for visual estimation of the aureole width  $\Delta\varphi$ . This width varies from a half to one and a half of the moon's radius. Let the position of the first zero of the Bessel function describing the aureole peak of the scattering phase function be taken as the width  $\Delta\varphi$  for a particle with a dimensionless radius  $\rho = 2\pi r/\lambda$  ( $\lambda$  is the light wavelength):  $\rho\Delta\varphi \simeq 4$ . Then, taking into account that the moon's radius  $\delta r \simeq 1/4^\circ \simeq 1/220$ , we obtain the following expression for the particles' radius:

$$r \simeq 130\lambda/\Delta\varphi, \quad (1)$$

where  $\Delta\varphi$  is given in units of the moon's radius.

The visual estimation corresponds approximately to  $\lambda = 0.5 \mu\text{m}$  what yields the value of the characteristic dimensions of the particles  $r \simeq 40-150 \mu\text{m}$ . Thus, the aureole peak of the brightness angular distribution is formed due to very large particles.

This paper consists of two main parts. The methodical part is devoted to the study of the possibilities of at least estimating the quantity of such particles. The other part contains the analysis of data on the brightness scattering phase functions of the sun aureole. The data were obtained during the complex cloud experiments at the Zvenigorod Measurement Site of the Institute for Atmospheric Physics in 1992 and 1994. The first section of the methodical part is devoted to the calculation of the instrumental function of the sun photometer, and the second section describes the adaptation of the inverse problem solution to the device.

The possibility of using the sun aureole method for studying translucent clouds was demonstrated in Ref. 1. There are formulated the requirements to the equipment and the restrictions upon the types of cloudiness. Let us remind that the sun aureole spectrophotometer was created as a device for studying the coarse tropospheric aerosol. Its main parameters are: four operating wavelengths  $\lambda_1 = 0.46; 0.54; 1.2; 1.55 \mu\text{m}$ ; operating angular range  $\varphi = 2-10^\circ$ ; angular scanning is discrete. The detection time of the spectral dependence (for  $\varphi = \text{const}$ ) is a few seconds, the full recording time (depending on the set of angles  $\varphi_j$ ) is not more than 5 min.

In dust emissions and background conditions, the size of particles that make noticeable contributions to

their total volume and optics, varies from a few tenth of micron to approximately 10–15  $\mu\text{m}$ , and the device's parameters well suit this size range. In translucent clouds, the dimensions of optically active particles vary from the fractions of a micron to hundred microns in Ci cloud, as it was shown above. "Pure" types of cloudiness (perhaps excluding Ci) are realized rather seldom, and usually one deals with a multilayer cloudiness of different types including cirrus as a rule. Thus, both experimental data and the technique of their conversion must at least recognize the presence of particles characteristic of Ci. We'd like to emphasize that these particles are obviously nonspherical, so one can estimate only the total volume of particles and the characteristic size even with an ideal device and technique. The inversion of aureole scattering phase function simulates real particles by spheres whose cross section is approximately equal to that of real particles. Their cross section is perpendicular to the sighting ray, i.e., it depends on the particles' orientation. The calculations in terms of the particles' volume (say, prisms or columns) can yield an error up to two times. Approximately the same error can appear in the characteristic size. The formula (1) shows two possibilities to extend the range of particles' dimensions, measurable with the device, to larger radii  $r$ . One may increase the maximum wavelength of the spectral range and decrease the initial angle  $\varphi_{\text{min}}$ . The first way is connected with a significant redesign of the device and is possible as a prospect. As for the second way, it is necessary to know whether the relation between the angular dimension of the Sun  $2\Delta v$  and the

initial angle  $\varphi_{\text{min}}/v \simeq 10$  (what is realized in our device), is a limiting value from the viewpoint of distortions of the angular behavior of the scattering phase function  $\mu(\varphi)$  recorded.

### THE INSTRUMENTAL FUNCTION OF THE SUN PHOTOMETER

The attempts to estimate the errors due to finite angular dimension of the source and the photometer's field of view in measuring  $\mu(\varphi)$  were made in several papers. In Ref. 2, the calculations were performed for the set of  $\mu(\varphi)$  for aerosol with the inversely power law of particle size distribution. The results were presented in the form that doesn't allow one to distinguish the influence of "angular divergence" of the "source – device" system. Our calculations were from the very beginning aimed at obtaining such a device characteristic that could be defined as the angular instrumental function  $A(\varphi - \varphi_0)$  of the "Sun – photometer" system. From its dependence on the angle  $\varphi_0$  (the angle between the photometer axis and the direction to the center of the Sun) and the device's field of view  $2\delta$ , one obtains a ground for the choice of the initial angle of the range  $\varphi_{\text{min}}$  and estimate the errors due to finite  $A(\varphi - \varphi_0)$  value. In principle, knowledge of  $A$  makes it possible to reconstruct the true angular behavior of brightness  $\mu(\varphi)$  from the measured one  $\mu^*(\varphi)$  using the classic definition of  $A(\varphi - \varphi_0)$

$$\mu^*(\varphi_0) = \int A(\varphi - \varphi_0) \mu(\varphi) d\varphi. \tag{2}$$

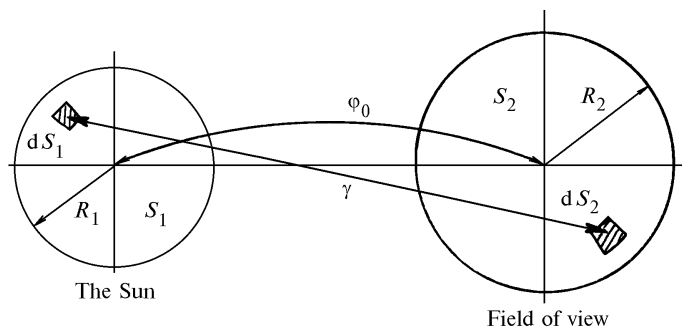


FIG. 1. The scheme for calculation of the instrumental function of the sun photometer. In the plane perpendicular to the sighting line from the Sun center to the photometer,  $R_1$  and  $S_1$  are the radius and the Sun projection area;  $R_2$  and  $S_2$  are the radius and the projection area of the photometer field of view;  $\varphi_0$  is the angle between the direction to the center of the Sun and the optical axis of the photometer;  $\gamma$  is the angle between the centers of the areal elements, i.e., the current scattering angle.

The general formula (2) for the recorded  $\mu(\varphi)$  can be considerably simplified in the domain of the sun aureole because the problem can be solved in a plane perpendicular to the line from the center of the Sun to the photometer by projecting the discs of the Sun and the photometer's field of view onto it (Fig. 1). Then we can introduce the following terms in the plane:

radius  $R_1$  and area  $S_1$  of the Sun, radius  $R_2$  and the area  $S_2$  of the photometer's field of view. For the value  $\mu^*$  averaged over the sun disc and the photometer's field of view we obtain

$$\mu^*(\varphi_0) = \frac{1}{S_1 S_2} \int_{S_1} dS_1 \int_{S_2} \mu(\gamma) dS_2. \tag{3}$$

The angle  $\gamma$  (see Fig. 1) is the "current" scattering angle between the irradiating element  $dS_1$  of the Sun and the element  $dS_2$  of the field of view. It is the function  $A(\gamma - \varphi_0)$ , the probability density function of the scattering angle  $\gamma$  at the scattering angle  $\varphi_0$ , is defined as the resulting or the full instrumental function of the "Sun - photometer" system. For brevity, we'll merely call it the instrumental function.

The calculation scheme was as follows. All the values  $\gamma$ ,  $\varphi_0$ ,  $R_2$  were measured in the units of the sun radius  $R_1$ . The domain of  $\gamma$  from  $\varphi_0 - 2R_1$  to  $\varphi_0 + 2R_1$  was divided into  $k$  intervals  $\Delta\gamma$ , and  $A(\gamma - \varphi_0)$  was determined as the frequency of  $\gamma$  being in the corresponding interval  $\Delta\gamma$  averaged over the areas  $S_1$  and  $S_2$ . Simultaneously,  $\mu^*$  and the mean value  $\langle\gamma\rangle$  were calculated for making a comparison by formulas from Ref. 2.

The sun photometer was designed so that the angular size of its field of view was  $2\delta \approx 35'$ , i.e., it was approximately equal to the angular diameter of the sun disc. This choice significantly simplified the scheme of the absolute ( $\text{sr}^{-1}$ ) calibration of the device. Analysis of the function  $A(\gamma - \varphi)$  calculated demonstrates that symmetry also plays a positive part in the formation of the instrumental function: the condition  $R_1 = R_2$  guaranteed the symmetry of  $A(\gamma - \varphi)$  in the whole range of scattering angles. As was mentioned in Ref. 1, symmetric instrumental functions distort the scattering phase functions to a lower degree as compared with the asymmetric ones, even for the cases of a very steep angular behavior of  $\mu(\varphi)$ . These errors are proportional to  $(\delta\varphi/\varphi)^3$  where  $\delta\varphi$  is the halfwidth of  $A(\gamma - \varphi)$  because the symmetry "extinguishes" even terms of the expansion of  $\mu(\varphi)$  into a series over  $\varphi$ .

The function  $A(\gamma - \varphi)$  was calculated for the angles  $\varphi_0 = 1; 1.5; 2; 4^\circ$  and the field of view radii  $R_2 = (1.0; 0.5; 0.3)R_1$ . One can see that the scheme from Fig. 1 is invertible with respect to  $R_1$  and  $R_2$ , so the variants of  $R_2 > R_1$  (the field of view is broader than the sun disc) can be obtained by scaling the angle  $\varphi_0$ .

Some of results calculated are presented in Fig. 2. Curves 1 and 3 are obtained for  $R_1 = R_2$  and  $\varphi_0 = 1^\circ$ ,  $\varphi_0 = 2^\circ$  respectively. The angle  $\gamma - \varphi_0$  is presented by the  $x$ -axis in the sun radius units (this makes it possible to join the curves  $A(\gamma - \varphi)$  for clearness). Figure 2 is an illustration to the fact that a statement evident on the face of it but not verified by a rigorous calculation can be false. It is the calculation of the instrumental function that permits one to state that the function is similar for the geometric scattering angles  $\varphi_0 = 1^\circ$  and  $\varphi_0 = 2^\circ$ , i.e., from the viewpoint of angular resolution of the device,  $\varphi_0 = 1^\circ$  can be used on the same basis as  $\varphi_0 = 2^\circ$ . The curves  $A(\gamma - \varphi)$  for larger scattering angles are not shown in the Figure as they merely coincide with  $A(\gamma - 2^\circ)$ . One can assume, to a great degree of accuracy, that the function  $A(\gamma - \varphi)$  may be approximated by a triangular shaped curve.

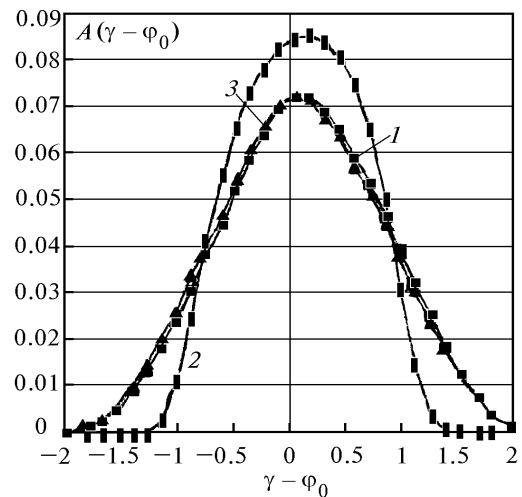


FIG. 2. Instrumental functions  $A(\gamma - \varphi_0)$  as functions of the geometric scattering angle  $\varphi_0$  and the relationship of angular size  $R_1$  of the Sun and the photometer field of view  $R_2$ .  $\varphi_0 = 1$  and  $2^\circ$ ,  $R_1 = R_2$  (1, 3);  $\varphi = 1^\circ$ ,  $R_2 = 0.3R_1$  (2).

The calculations of the instrumental function have revealed one of the causes of the distortions of the brightness angular distribution  $\mu(\varphi)$ : the weighted mean scattering angle  $\langle\gamma\rangle$  is always greater than  $\varphi_0$ . Their difference increases with a decrease in  $\varphi_0$  relatively and absolutely. For  $\varphi_0 = 1^\circ$ , it is about 5 minutes of arc. The cause of this effect can be easily understood from Fig. 1.

The interference from direct solar radiation scattered in the device is one more reason to restrict ourselves by the value  $\varphi_{\min} = 2^\circ$  in the choice of the initial angle  $\varphi_{\min}$ . This noise rapidly (almost exponentially) increases with a decrease of the scattering angle. It was possible to reduce the interference level to a few hundredths of  $\text{sr}^{-1}$  in terms of  $\mu(\varphi)$ . For  $\varphi = 1.5^\circ$ , the illuminating level is about a tenth of  $\text{sr}^{-1}$ , and for  $\varphi = 1^\circ$ , it is two or three tenths of  $\text{sr}^{-1}$ . Under conditions of clear sky, it is a significant error, but this interference is tolerable for the scattering phase functions  $\mu(\varphi)$  of clouds whose level is a few units for  $\varphi = 1^\circ$  as the minimum.

The curve 2 in Fig. 2 is calculated for the photometer whose field of view  $R_2 = 0.3R_1$ . It is easy to see that a significant (three-fold) narrowing of the photometer's field of view insignificantly decreased the halfwidth of the instrumental function but a considerably deformed the function: the shape of  $A(\gamma - \varphi)$  became closer to rectangular with a very pronounced asymmetry.

At  $R_2 \rightarrow 0$  we have a narrow-angle photometer whose field of view is much less than the angular size of the Sun. The instrumental functions corresponding to this scheme (Fig. 3) were calculated for the angles  $\varphi_0 = 1^\circ$  and  $2^\circ$ . Both curves have strong asymmetry, the maximum of  $A(\gamma - \varphi)$  is also displaced to larger angles, and its halfwidth slightly differs from that in

the scheme with  $R_1 = R_2$  and equals approximately to a quarter of a degree.

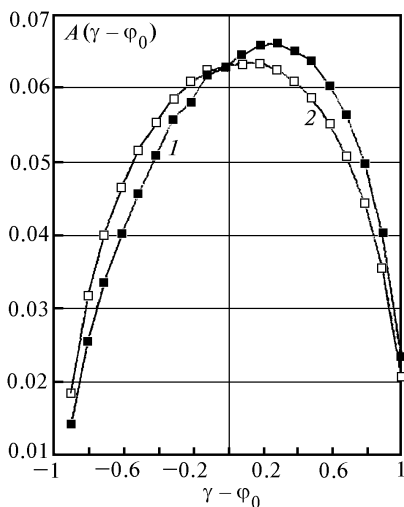


FIG. 3. Instrumental functions of the narrow angle ( $R_2 \approx 0$ ) photometer  $\varphi_0 = 1^\circ$  (1);  $\varphi_0 = 2^\circ$  (2).

Distortions introduced by instrumental function of the described types were analyzed for the aureole portion of the scattering phase function using several distributions simulating large- and small-drop clouds in the range of modal drop dimensions  $r = 3\text{--}30 \mu\text{m}$ . The function  $\mu(\gamma)$  is very steep and its tabular definition yields a great error in calculations because the angle  $\gamma$  varies almost continuously. So, to improve the accuracy of calculations in the angle range  $\gamma = 0\text{--}10^\circ$ , interpolation polynomials were constructed for model  $\ln(\mu(\gamma))$ .

The comparison of calculated  $\mu^*$  performed by formulas (3) and (2) demonstrated that they coincide up to a few tenths of a percent. Since the question on the accuracy of the approximation for Fig. 1 ("plane" geometry) was still open, the calculations by this scheme were compared with those performed by rigorous formulas<sup>2</sup> by M.A. Sviridenkov. The estimations of  $\mu^*(\varphi)$  yielded the same type of distortion by the device for three scattering angles: the overestimation of  $\mu^*$ . These estimations differed not more than by 1–2%. So the correctness of the scheme in Fig. 1 was justified. As to distortions caused by imperfectness of  $A(\gamma - \varphi)$ , they were not more than +5% for most of conceivable scattering phase function of a cloud at the angle  $\varphi = 1^\circ$ . The errors decrease with the increase of the scattering angle.

Let us summarize the first part of the section. The exact calculation of the brightness angular behavior averaged over the sun disc and the field of view of the photometer and its determination by simple convolution of  $\mu(\varphi)$  with the instrumental function of the device yield coinciding results. The errors introduced by  $A(\gamma - \varphi)$  add up to five percent in detecting brightness angular behavior with a steep angular behavior (of the cloud type). The symmetric scheme when the angular dimensions of the field of

view and the sun coincide is optimal for the photometer. In this case the shape and halfwidth of the function  $A(\gamma - \varphi)$  in fact do not depend on the scattering angle up to  $\varphi = 1^\circ$ . This makes it possible to widen the range of operating angles of solar photometers to  $\varphi = 1^\circ$ . The maximum of the instrumental function (and the weighted mean of the scattering angle  $\langle \gamma \rangle$ ) is always shifted to larger angles  $\varphi$  (as the effective angle  $\gamma$  is displaced to smaller  $\varphi$  for rapidly decreasing  $\mu$ ). The shift is about a few angular minutes and decreases with the increase of the angle  $\varphi$ . The instrumental functions become asymmetric for narrow-angle photometers but their halfwidth decreases insignificantly; in principle, knowledge of  $A(\gamma - \varphi)$  allows one to reconstruct the true behavior of  $\mu(\varphi)$ .

In conclusion, let us note that the use of as small angles as possible is preferable for the reasons of decreasing errors due to multiple scattering.<sup>5</sup>

### THE TECHNIQUE OF THE INVERSE PROBLEM SOLUTION

Thus, the range of size of large cloud particles detectable with a photometer turned out to be twice as wide as compared with the initially supposed. But the examination of earlier inversion results required accurate analysis of methods and possibilities for inversion of the brightness in aureole angular region. The range of particle size for which the kernel of the inverse problem  $K_{ij}$  was calculated, the discretization, and the number of points in the division of the interval  $\Delta r$  were developed in model calculations of  $\mu(\varphi)$  for narrow lognormal distributions with  $v^2 = 0.05\text{--}0.1$  (sonde distributions). First of all, it was necessary to find the boundary of the size region where large particles can yet be distinguished. By this boundary, we mean the following. The structure of the kernel  $K_{ij}$  is as follows: the first measurement of the matrix  $K_{ij}$  (conventionally, the line  $i$ ) forms a set of four wavelengths for five scattering angles (total,  $m = 20$ ), the second one forms the columns  $j$ , i.e. radii  $r_j$  of the division points for the range of reconstructed dimensions for the distribution of volumes  $V(r_j)$ . The calculations of  $K$  demonstrated that, for the standard angle set  $\varphi = 2\text{--}10^\circ$ , the lines become quasiparallel (i.e., proportional) already at  $r_j > 50$  even for  $\Delta r_j = 10\text{--}15$ , and the dependence on  $\lambda$  and  $\varphi$  weakens in the lines. Mathematically, this means that the problem is ill-posed; physically, this means that the particles from the size intervals  $\Delta r_j$  and  $\Delta r_{j+1}$  of the distribution  $V(r)$  are indistinguishable. It is evident that this appears as early as the measurement errors in  $\mu(\varphi)$  become large. One of the inevitable causes of the errors is the discretization of the kernel of the initial equation of the inverse problem. So, even the exact theoretically calculated  $\mu(\varphi, \lambda)$  will be reconstructed with an error depending on the discretization step, and narrow distributions will be distorted stronger.

Figure 4 presents the results of a numerical experiment. The parameters of the model lognormal distributions  $r_{\text{mod}} = 5, 15, 30 \mu\text{m}$ ; the halfwidths are  $v^2 = 0.05, 0.1, 0.05$ , respectively. The range of radii  $r = 0.3\text{--}60 \mu\text{m}$  was divided into twenty intervals. For such a broad domain, this should be considered as a coarse division, especially if we take into account that the sonde distributions are narrow. Nevertheless, the inversion sufficiently well reproduces the main characteristics (the position of the mode and halfwidth) for all the three distributions including that for large droplets one. The total volume of particles was reconstructed accurate to 10–15%. The principle conclusion that is evident from Fig. 4 is as follows. The domain of the kernel  $K$  can be extended to  $\approx 50\text{--}60 \mu\text{m}$ , even for the same parameters of the device. If the measurement error for  $\mu(\varphi)$  does not exceed  $\approx 10\text{--}15\%$ , the diagnostics of the largest particles (determination of the mode position and the distribution width) is possible with the only remark that we deal with nonspherical particles. The domain of the kernel and the measurement error are closely related, and the increase of the latter narrows the former.

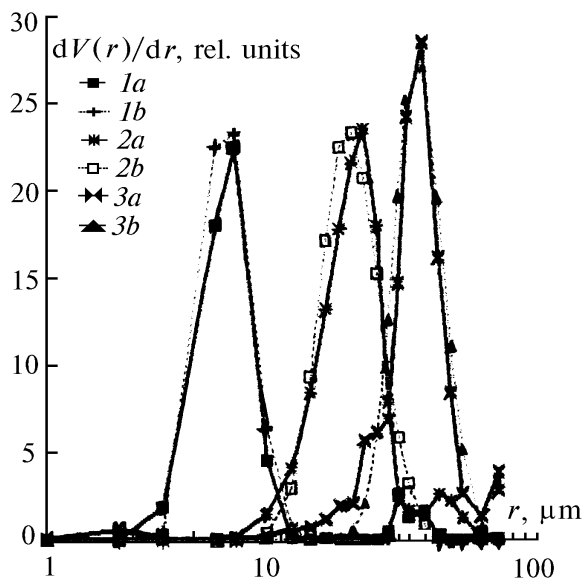


FIG. 4. The results of numerical experiment on reconstruction of narrow particle size distribution. The index “a” refers to the initial  $V(r)$ , “b” means the reconstructed ones. Median radii are  $r = 5$  (1), 15 (2), and  $30 \mu\text{m}$  (3).

The appearance of a quasi-periodic set of false maxima in the reconstructed  $V(r)$  is an interesting lateral effect of reconstruction of narrow distributions by coarse kernel discretization. Their amplitude is a few percent of the main maximum. The picture seems like a distortion of a rectangular shaped pulse with the loss of high-frequency spectral components (a coarse division is just the loss of high frequencies).

Let us consider some specific features of the iteration method for inverting of optical information. Of course, one can think that the guaranteed positiveness of the solution (in contrast to the Turchin<sup>3</sup> method) is an advantage of the method. However, it is necessary to note the following. On the basis of Turovtseva’s method of statistical regularization, an inversion algorithm was realized. In this algorithm, the positiveness condition is imposed at the final stage of the solution of inverse problem. This algorithm was used in Ref. 4. In this operation, the narrow domain of weakly negative values of the reconstructed distribution function (a few percent of the maximum) was transformed into a dip (down to 30%) near the vertex of the distribution. In other words, the false irregularity is a side effect of the condition of non-negativeness. To weaken this effect, it is necessary to use a sufficiently strong regularization in the iterative method.<sup>6</sup> The simplest way was to smooth the correcting factor, i.e., the correction of the reconstructed distribution.

Let us remind the main idea of the algorithm.<sup>6</sup> The correction  $Q(r)$  to the distribution reconstructed is as follows:

$$Q(r_i) = \frac{\sum_j \mu_j K_{ij}}{\sum_j \mu_j^* K_{ij}}, \tag{4}$$

where  $\mu_j^* = \sum_i N(r_i) K_{ij}$  is the optical information vector reconstructed using the distribution  $N(r_j)$  obtained at the previous step. It is the correction  $Q(r)$  that we smoothed using sliding average after each iteration. At the same time an additional factor

$$\delta(r_i) = 1 - \frac{1}{n} \left( \frac{m - 2i}{m} \right)^4 \tag{5}$$

close to unity was added to the corrector (the factor is an element of *a priori* information). Here  $m$  is the number of discretization points;  $n$  is the number of iterations. This factor provides the check of a natural condition that the unknown distribution must rapidly decrease at the boundaries of the size range.

According to the analysis, this regularization considerably smoothens the obtained solution and deteriorates the accuracy of reconstruction for  $\mu$  only by 2–3%. After already  $\approx 30$  iterations the deviation of the correcting factor from unity does not exceed 0.01; after 100 iterations,  $\approx 0.001$ . Then, we restricted the number of iterations by  $n = 50\text{--}100$ .

### ANALYSIS OF THE MEASUREMENT RESULTS

The angular behavior of brightness of the sun at the aureole angles was recorded both during the cloud experiment and some time after its end. Before September, 1994 we used the previous set of the scattering angles, then we added the angle  $\varphi = 1.5^\circ$  to this set. To use  $\varphi = 1^\circ$ , a modification of the device tracking system would be necessary. It is

necessary for decreasing the residual error of tracking the sun at different optical thicknesses of clouds. Analyzing the inversion curves  $V(r)$ , we'll keep in mind two side effects of the inversion algorithm: the ripples and dips near the distribution maximum are often the effects of the solution's positiveness, and the small false maxima following the main narrow peak of  $V(r)$  are effects of the coarse discretization.

First of all, we have revised the previous measurement data including those presented in Ref. 1. To invert the data obtained earlier, mainly during the preceding cloud experiment (1992), we applied the modified inversion algorithm and the kernels  $K$  extended to  $r = 60 \mu\text{m}$ . Some examples of the distribution densities of volumes  $V(r)$  with respect to particle size are presented in Fig. 5. The curves 1 and 2 (Fig. 5a) correspond to the curve 1 in Fig. 3a and curve 3 in Fig. 3b,<sup>1</sup> the curve 3 in Fig. 5a corresponds to curve 2 in Fig. 2.<sup>1</sup> The comparison of the distributions  $V(r)$  obtained with a "short" and "extended" kernel demonstrates that the former displaces the distribution maximum to smaller radii  $r$ , and somewhat overestimates the concentration of particles with the radii at 6–10  $\mu\text{m}$  in order to compensate for the displacement. In all cases, the displacement is less than 30%, i.e., the distribution is not distorted too strongly on the whole. As to the total volume of particles, the difference is two-fold (due to the appearance of larger particles in the distribution).

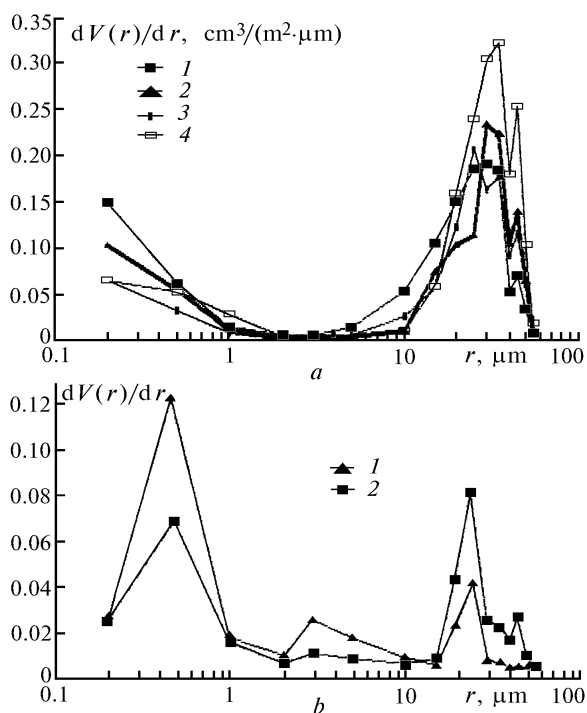


FIG. 5. The results of inversion for data of 1992: a) one-layer cloudiness of Ci type (1, 2, 3); As cloudiness (4); b) aircraft track.

The results of inversion obtained for the scattering phase function of a very homogeneous and

rather dense ( $\tau \approx 0.7$ ) As clouds (curve 4 in Fig. 5a) turned out to be rather unexpected (i.e., it was As where the scattering dominated). The homogeneity of the cloudiness made it possible to use the complete set of the angles  $\phi_j$ , and the reconstruction error turned out to be extremely small, about 5%. It is normally accepted that the mode of the  $V(r)$  distribution in As is approximately in the range  $r \approx 10 \mu\text{m}$ , here, the distribution maximum falls within the range  $r \approx 25\text{--}30 \mu\text{m}$ . Let us note a very large number of submicron particles, however, this can be partly caused by the effects of multiple scattering.

Figure 5b presents the inversion results for  $\mu(\phi, \lambda)$  belonging to a deteriorated and sufficiently homogeneous aircraft track. The track was carried at a small angle to its axis, so we could obtain two records at a temporal interval of 10 min, so the two curves in Fig. 5b also presents two stages of the track development to a certain extent. One can see three modes in the distribution. The modes are the powerful submicron, relatively weakly pronounced three-micron, and the mode of large particles at 20–25  $\mu\text{m}$ . During the temporal interval  $\approx 10$  min, the fine and medium size particles were as if transferred into large ones.

Now let us return to the analysis of the results obtained during the complex cloud experiment in 1994. All in all, during June – September of 1994, nine episodes of translucent cloudiness were observed: four in June, two in July, and three in September. Excluding the episode on September, 26, the cirruses were normally present: one-layer Ci, or together with As or Ac, or two layers of Ci (the situation with the double tropopause). The cloudiness characteristics mostly changed rapidly (first of all, the optical thickness  $\tau$ ) so we had to use an incomplete set of scattering angles (first three or four angles  $\phi_j$ ). For the number of discretization points  $n = 16$  the problem is undefined, but the degree of arbitrariness is not high. Several records were obtained in every episode. To arrange more than twenty curves in the figures was not an easy task since close situations superimpose. If the level of curves differs too much, the details of curves are lost, while the use of the double logarithmic scale leads to the loss of clearness.

It is too early to speak about regularities based on only nine episodes, but one can at least plan the further study. Some generalizing conclusions may obviously be drawn based on the analysis of Figs. 5 and 6. For the case of one-layer cirruses (see Fig. 5a, curves 2, 3; Fig. 6b, f), volume distributions  $V(r)$  are narrow and single-mode. The position of the mode varies in the range  $r = 20\text{--}40 \mu\text{m}$ . The fraction of small particles ( $r \approx 1\text{--}3 \mu\text{m}$ ) is absent or only weak. In two-layer cloudiness of Ci+Ci type, the distributions with different parameters are observed in two layers, so the resulting distribution is either double-peaked (curves 1, 2, 3 in Fig. 6a) or wider due to coincidence of the peaks. If we have the case of the cloudiness of the Ci+As type, the result depends on the relation of the layer's optical

thicknesses: if As dominates in the scattering, there are observed distributions similar to the curve 4 in Fig. 5a; if the contributions of As and Ci are close, we obtain an intermediate type (curves in Fig. 6e) with a plane distribution vertex and considerably larger halfwidth. The episode of September 26, curve 2 in Fig. 6c, is significant (as it is written in the caption, the lower cloudiness layer is identified as a dense one. However, the halo ring was distinctly

seen around the sun. This unambiguously indicates the presence of the upper Ci layer in which large ice crystals prisms) exist. The maximum of the curve 2 falls at  $r = 45 \mu\text{m}$ ; it is not excluded that real  $r$  is larger and the effect is explained by small size  $r_{\text{max}}$  in the kernel  $K$  and specific features of the algorithm. The bell at  $r \approx 30 \mu\text{m}$  resembles the curve 4 in Fig. 5a; in other words, the contributions of As and Ci for this episode are near the resolution limit.

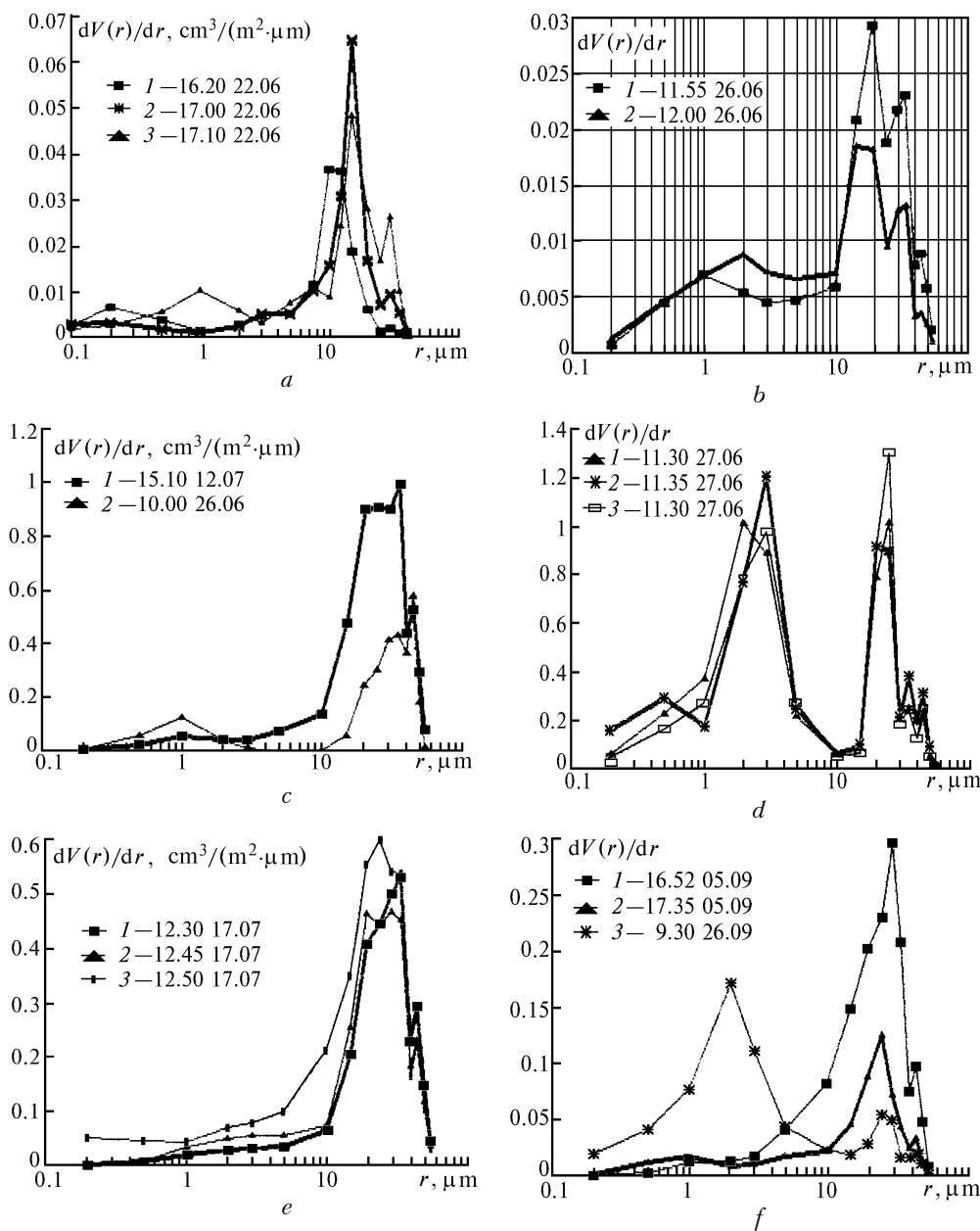


FIG. 6. Results of inversion made using the data of 1994: a) June 22, Ci+Ci+Ac, time 16.20–17.20; b) June 25, Ci, time 11.50–12.00; c) Ci+As cloudiness: July 12, time 15.00 (1); June 26, time 10.00; d) Ci+Ac, June, 27, time 11.30–11.45; e) Ci+As, July 17, time 12.30–12.50; f) one-layer cloudiness: Ci, September 5, time 16.25–17.35 (1, 2); Ac, September 26; time 9.30 (3).

The presence of a rather powerful Ac layer under the Ci layer in the distribution  $V(r)$  generates the

second bell in the size range  $r \approx 1-3 \mu\text{m}$ , Fig. 6d. It is worth drawing attention to a remarkable

reproducibility of the curves  $V(r)$ : the third curve was recorded after a quarter of an hour after the first one. A very narrow fraction belonging to cirrus has the modal size  $r \simeq 25 \mu\text{m}$ . The modes are separated by a deep and wide dip. Comparison with Fig. 6f enables one to assume that the situation presented in Fig. 6d is sufficiently characteristic. Both distribution fractions are presented in Fig. 6f in a pure form, i.e., separately (the curves refer to different episodes, September 5 and 29). The curve 1 belongs to thin one-layer Ac clouds, and the curves 2 and 3 belong to thin one-layer cirrus. So, the curves from Fig. 6d can be constructed using the curves from Fig. 6f. In other cases, the picture is not so distinct: the Ac bell is weak (curve 1 in Fig. 6a).

The total volume of particles (i.e., the water or ice content) within the size range  $r = 0.3\text{--}60 \mu\text{m}$  varied approximately from 1 (for the thinnest Ci at  $\tau \simeq 0.2$ ) to 20 (at  $\tau \simeq 1$ ) cubic centimeters (for water, grams) per  $1 \text{ m}^2$ .

Thus, the determination of cloudiness types by the traditional classification (it was performed by employers of the Department of Geography, Moscow State University, during the experiments), with

respect to the number of layers, layer type, well agrees with the characteristics of the particles' volume distribution curves. So one can expect that the sun aureole method is able to give sufficiently reliable information on the size distribution of cloud particles provided that the above stated remarks on Ci clouds are kept in mind.

#### REFERENCES

1. A.A. Isakov, *Izv. RAN, Fiz. Atmos. Okeana* **30**, No. 2, 246–251 (1994).
2. M. Shiobara, T. Nayasaka, T. Nakajima, and Tanaka, *J. of the Meteorol. of Japan* **7**, No. 1, 65–69 (1991).
3. V.F. Turchin, *Izv. Akad. Nauk SSSR, Fiz. Atmos. Okeana* **9**, No. 10 (1973).
4. G.I. Gorchakov, A.A. Isakov, and L.S. Turovtseva, in: *The Second All-Union Symposium on Atmospheric Optics* (Tomsk, 1976), pp. 85–88.
5. E.P. Zege, et al., *Izv. RAN, Fiz. Atmos. Okeana* **30**, No. 3, 328–336 (1994).
6. J.T. Twitty, *J. Atm. Sci.* **32**, No. 3, 584–591 (1975).